Chem

CellPress

Article

Bio-inspired Molecular Redesign of a Multi-redox Catholyte for High-Energy Non-aqueous Organic Redox Flow Batteries

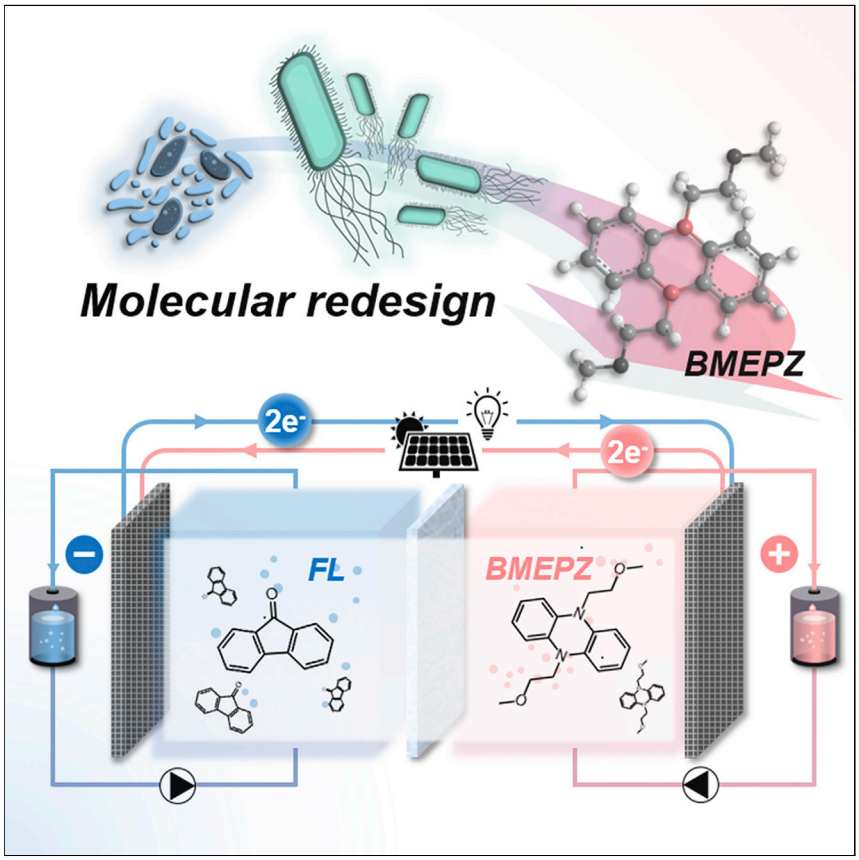

A highly soluble and multi-redox phenazine-based molecule, BMEPZ, is redesigned through bio-inspiratioin as high-performance catholyte material for NORFBs. A full-flow RFB based on BMEPZ/FL redox couple exhibits cell voltage of 1.2 and 2.0 V and stable cycling. The highest energy density among NORFBs is attained based on the multi-redox capability and high solubility.

Giyun Kwon, Kyunam Lee, Myeong Hwan Lee, ..., Soo Young Park, Ji Eon Kwon, Kisuk Kang

mracle2@snu.ac.kr (J.E.K.)
matlgen1@snu.ac.kr (K.K.)

HIGHLIGHTS

Highly soluble and multi-redox BMEPZ for non-aqueous redox flow batteries

Investigation of kinetic properties and redox mechanism of BMEPZ

The highest energy density among non-aqueous all-organic redox flow batteries

Bio-inspired molecular redesign of high-performance catholyte material

Kwon et al., Chem 5, 2642–2656
October 10, 2019
https://doi.org/10.1016/j.chempr.2019.07.006

Chem

CellPress

Article

Bio-inspired Molecular Redesign of a Multi-redox Catholyte for High-Energy Non-aqueous Organic Redox Flow Batteries

Giyun Kwon,[1,3] Kyunam Lee,[2,3] Myeong Hwan Lee,[1] Byungju Lee,[1] Sechan Lee,[1] Sung-Kyun Jung,[1] Kyojin Ku,[1] Jihyeon Kim,[1] Soo Young Park,[2] Ji Eon Kwon,[2,*] and Kisuk Kang[1,4,*]

SUMMARY

Redox-active organic materials (ROMs) have recently attracted significant attention for redox flow batteries (RFBs) to achieve green and cost-efficient energy storage. In particular, multi-redox ROMs have shown great promise, and further tailoring of these ROMs would yield RFB technologies with the highest possible energy density. Here, we present a phenazine-based catholyte material, 5,10-bis(2-methoxyethyl)-5,10-dihydrophenazine (BMEPZ), that undergoes two single-electron redox reactions at high redox potentials (−0.29 and 0.50 V versus Fc/Fc^+) with enhanced solubility (0.5 M in acetonitrile), remarkable chemical stability, and fast kinetics. Moreover, an all-organic flow battery exhibits cell voltages of 1.2 and 2.0 V when coupled with 9-fluorenone (FL) as an anolyte. It shows capacity retention of 99.94% per cycle over 200 cycles and 99.3% per cycle with 0.1 M and 0.4 M BMEPZ catholyte, respectively. Notably, the BMEPZ/FL couple results in the highest energy density (~17 Wh L^{-1}) among the non-aqueous all-organic RFBs reported to date.

INTRODUCTION

With the ever-increasing global demand for the development of greener and sustainable energy sources to mitigate the environmental concerns associated with fossil fuels, renewable energy sources such as solar and wind power are becoming affordable and broadly deployed. To achieve round-the-clock energy delivery, however, these power sources must be paired with scalable energy storage systems (ESSs) owing to the significant mismatch between the energy supply and demand.[1,2] Redox flow batteries (RFBs), which utilize redox-active materials dissolved in separate electrolytes, are considered some of the most promising ESSs for modern grid markets, and decoupling the energy and power is regarded facile for RFB systems.[3–8] With the aim of pursuing the development of green energy technology, research on RFBs has also shifted from conventional metal-based redox-active materials such as vanadium and zinc to redox-active organic materials (ROMs), which are naturally abundant and potentially cost effective, safe, and chemically tunable.[9–11] In particular, recent studies on non-aqueous all-organic RFBs (NORFBs) have demonstrated the great promise for achieving high energy densities in these systems without the concerns associated with water electrolysis, which typically limits the working voltage to a narrow range and thus leads to a rather low energy density in aqueous RFBs.[12–17]

Despite the great potential of organic RFBs, their practical energy density remains very low.[10] The energy density of ROM-based RFBs is dependent on the following

The Bigger Picture

Ever-growing attention to environmental preservation has accelerated the global shift toward renewable energy. However, complete replacement of fossil fuel is yet impossible because of intrinsic intermittency of renewable energy. Thus, large-scale energy storage systems with safety and cost-effectiveness are necessary to solve this limitation. Non-aqueous all-organic redox flow batteries (NORFBs), which store energy in redox-active organic materials (ROMs) dissolved in non-aqueous solution, have received massive attention as promising candidates for this application. Current development of NORFBs is hindered by limited choices and performances of ROMs. We present the BMEPZ/FL system delivering the highest energy density among NORFBs. We discuss the redesign of the catholyte material, BMEPZ, based on inspiration from biosystems. Our results of multi-electron redox material at high potentials with enhanced solubility provide a breakthrough in the realization of high-energy-density RFBs.

three factors: (1) the selection of the anolyte and catholyte and their corresponding redox potential difference, (2) the amount of ROMs dissolved, and (3) the number of electrons participating in the redox reaction per ROM. Extensive research in recent years has led to the identification of various promising ROMs, such as quinone and viologen derivatives, that can be used as anolytes (i.e., n-type or reduction type).[18–27] For these anolyte ROMs, remarkable performance enhancements in terms of the solubility and multi-electron redox activity have been achieved.[23,26,28,29] Nevertheless, only a limited number of ROMs have been reported as promising catholyte materials (i.e., p-type or oxidation type).[8,30] Research on these p-type (oxidation type) ROMs is still in its infancy, and high-energy organic RFBs can only be realized when anolytes are coupled with appropriate catholytes.[12,25,31,32] Moreover, p-type ROMs capable of multi-electron redox reactions are even rarer because their oxidized states, such as dications, are often highly unstable in a solution.[13]

Considering a realistic limit of the ROM concentration in non-aqueous media,[15,33] exploiting multi-electron redox from a single p-type ROM is indispensable to achieve high energy density at a given concentration.[34] Several attempts have very recently been made to utilize multi-electron redox p-type ROMs as catholytes.[35–37] For instance, Kowalski et al. demonstrated that the chemical stability of the dication state of phenothiazine-based molecules can be enhanced by introducing methoxy groups at the para positions to the nitrogen atom of the phenothiazine core. Accordingly, the second redox reaction of the phenothiazine catholyte can be utilized reversibly in a non-aqueous bulk-electrolysis cell.[36] However, critical challenges in multi-electron redox catholyte ROMs must be addressed, such as their low solubility (< 0.1 M) and lack of long-term stability in the flow cell.[36,37] To realize high-energy-density RFBs, there is thus an urgent demand for the development of new p-type ROMs capable of stable and reversible multi-electron redox that exhibit high solubility.

In this report, we present a high-energy-density NORFB by exploiting a multi-electron redox p-type ROM as a catholyte; this ROM was rationally designed by mimicking the energy transduction in living organisms. This newly synthesized phenazine-based molecule, 5,10-bis(2-methoxyethyl)-5,10-dihydrophenazine (BMEPZ), undergoes double-redox reactions at high redox potentials with enhanced solubility in non-aqueous media. Its redox mechanism is carefully investigated using spectroscopic tools combined with a computational method. Its multi-electron redox reactions are revealed to be remarkably reversible in acetonitrile (MeCN) solution and highly stable in all redox states. In addition, this molecule outperforms previously reported ROMs in terms of its mass- and charge-transfer kinetics. A full-flow RFB, in which BMEPZ is dissolved as a catholyte at concentrations of up to 0.4 M, is prepared and it exhibits stable cycle performance, delivering the highest energy densities (~17 Wh L^{-1}) among NORFBs reported thus far. We believe that our material design can pave the way for the practical use of NORFB by reducing its performance gap with the state-of-the-art vanadium-based RFBs and aqueous all-organic RFBs (AORFBs).[38–40]

RESULTS AND DISCUSSION

Bio-Inspired Redesign of Catholyte Material

In biosystems, common redox-active molecules are known to undergo multi-electron redox reactions in the electron transport chains. Among such biological redox systems, methanophenazine is known to act as a redox mediator in a respiratory

[1]Department of Materials Science and Engineering, Research Institute of Advanced Materials (RIAM), Seoul National University, 1 Gwanak Road, Seoul 151-742, Korea

[2]Center for Supramolecular Optoelectronic Materials (CSOM), Department of Materials Science and Engineering, Research Institute of Advanced Materials (RIAM), Seoul National University, 1 Gwanak-ro, Gwanak-gu, Seoul 08826, Korea

[3]These authors contributed equally

[4]Lead Contact

*Correspondence: mracle2@snu.ac.kr (J.E.K.), matlgen1@snu.ac.kr (K.K.)

https://doi.org/10.1016/j.chempr.2019.07.006

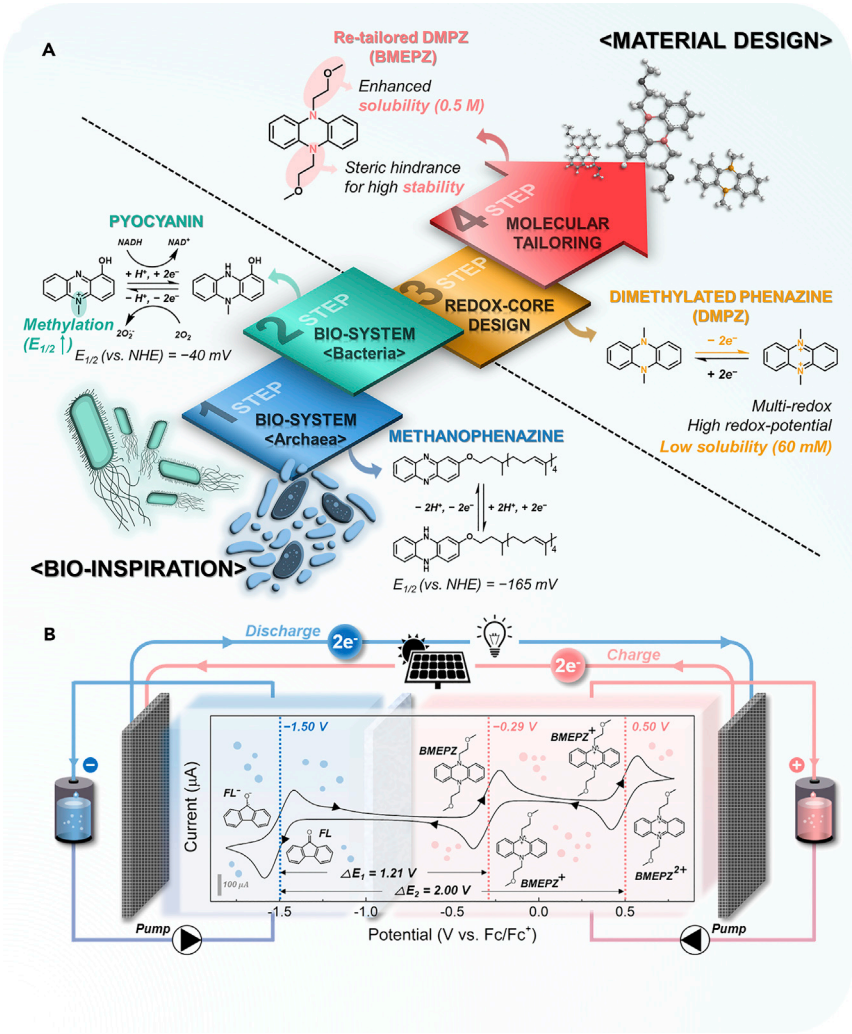

Figure 1. A New Multi-electron Redox Catholyte Material with Enhanced Solubility, BMEPZ

(A) The rational molecular design strategy of BMEPZ inspired by biological redox systems.

(B) Schematic illustration of all-organic full-flow battery containing BMEPZ/FL electrolytes and CV curves of the redox couple at a scan rate of 100 mV s^{-1}.

chain of archaea *Methanosarcina mazei* Gö1.[41] The methanophenazine can transport two electrons accompanying translocation of two protons through reversible reduction reactions (see Figure 1A).[42] The redox core structure of the methanophenazine consists of a pyrazine core bearing two imine-like nitrogen (–N=) atoms. By accepting two electrons with two protons, the pyrazine core is reduced to form a dihydrophenazine (see the core structures and details of the redox reactions in Figure S1A), offering a redox potential of approximately −165 mV versus NHE. Because of its suitable potential as an anolyte, several derivatives possessing the pyrazine core were recently utilized as anolytes for AORFBs coupled with a $Fe(CN)_6$ catholyte.[43] Pyocyanin, a redox-active molecule involved in the electron-transfer reactions of *Pseudomonas aeruginosa* bacteria,[44] bears a similar core structure as methanophenazine but has a substituent in the core, delivering much higher redox potential in its deprotonation of NADH (Figures 1A and S1B).[45,46] Similar to the pyrazine core, the methylpyrazinium moiety as a redox core also undergoes a reduction by two electrons; however, only one proton is involved to form a methyl-hydropyrazine

because the quaternized N can be reduced to a tertiary amine-like N without a proton. In contrast to the proton compensation for the pyrazine/dihydropyrazine couple, this methylated-pyrazine-core redox couple (i.e., methylpyrazinium/methyl-hydropyrazine) can bear a positive charge in its oxidized form.

Comparison of these two bio redox systems led us to speculate that the absence of the charge-relief process resulting from methylation likely leads to a higher redox potential ($E_{1/2}$ = −40 mV versus NHE) of pyocyanin,[46] and we anticipated that an additional methylation on the other imine-like N of the pyrazinium core would further increase the redox potential. Indeed, we observed that 5,10-dimethyldihydrophenazine (DMPZ) could undergo redox reactions at higher potentials ($E_{1/2}$ = −0.26 and 0.50 V versus Fc/Fc^+, ~0.40 and 1.16 V versus NHE, see Figure S1C) between a dimethylpyrazine dication/dimethylpyrazine redox core couple.[37,47] Moreover, because of the increased redox potential, in contrast to methanophenazine and pyocyanin, DMPZ naturally exists in its reduced form (neutral form) and reversibly undergoes two stepwise single-electron oxidations to form a stable dication (i.e., p-type redox) and is thus suitable for use as a catholyte. Nevertheless, the intrinsically low solubility of DMPZ (~60 mM in MeCN) has been a critical bottleneck for its practical application in RFBs.[37] Despite its high redox potential and multi-electron redox capability, the actual energy densities of RFBs employing DMPZ as a catholyte are far from practical application.

To this end, we attempted to re-tailor the DMPZ molecules to improve their solubility while maintaining the reversible and stable redox capability and succeeded in obtaining a new derivative, BMEPZ, that bears two flexible 2-methoxyethyl chains instead of the methyl groups (see step 4 in Figure 1A). It was expected that the flexibility and bulkiness of the alkyl ether chains would not only improve the solubility but also enhance the stability of the dication form by spatially hindering the redox-active N atoms from undergoing side reactions.[48–50] Synthesis of BMEPZ was performed starting with the reduction of phenazine using $Na_2S_2O_4$, followed by N-substitution of both amino groups with 2-chloroethylmethyl ether. The molecular structure of the synthesized BMEPZ was characterized using nuclear magnetic resonance (NMR) spectroscopy, high-resolution mass spectroscopy (HRMS), and elemental analysis (see the Experimental Procedures and Figure S2 for the synthetic details and reaction schemes). The newly synthesized BMEPZ exhibited enhanced solubility in MeCN as high as 0.5 M, which is one order of magnitude greater than that of the original DMPZ. To confirm that the substitution that improved the solubility did not reduce its original redox capability, we conducted cyclic voltammetry (CV) measurements of BMEPZ in MeCN solution. As shown in Figure S3, BMEPZ displayed two reversible redox peaks at voltages of −0.29 and 0.50 V versus Fc/Fc^+, which are identical to those of DMPZ. The electrochemical properties of BMEPZ will be discussed in further detail in the following sections.

To construct the all-organic RFB, the commercially available 9-fluorenone (FL) was employed as a typical anolyte ROM; FL undergoes an n-type redox reaction at −1.50 V versus Fc/Fc^+.[12] Because FL is highly soluble and undergoes one-electron redox reaction with good reversibility in MeCN, we could avoid unnecessary complexity in evaluating the redox activities of BMEPZ in the flow cell.[12] Figure 1C shows the redox activities of BMEPZ and FL in a mixed electrolyte along with the molecular structures for the corresponding redox states. In the CV measurement, the mixed electrolyte showed three reversible redox peaks with redox potentials and current levels identical to those of the corresponding redox peaks of each material in the separate electrolytes (Figure S3). Thus, the redox behaviors of the two ROMs

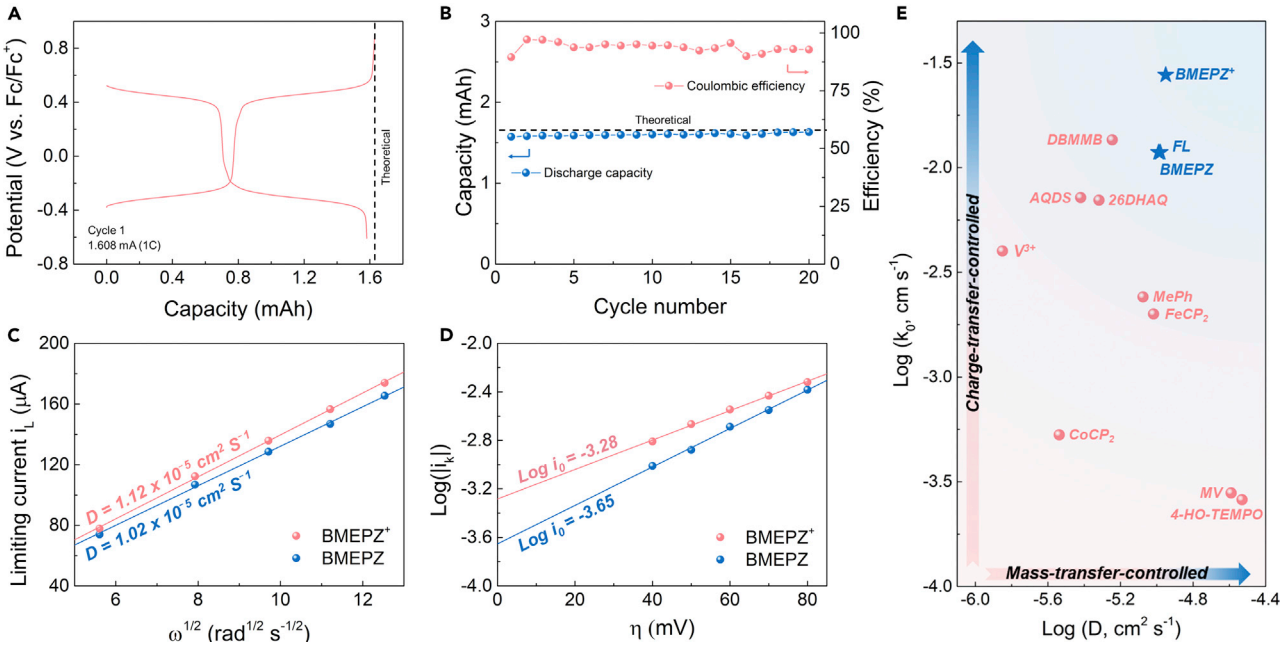

Figure 2. Characterization of BMEPZ

(A) Representative charge-discharge curve for bulk-electrolysis test of BMEPZ.

(B) Coulombic efficiencies and capacities for bulk-electrolysis test of BMEPZ with respect to cycle number.

(C) Linearly fitted Levich plots of limiting current (i_L) as a function of the square root of the rotation rate ($\omega^{-1/2}$).

(D) Linearly fitted plots of logarithm of kinetics-controlled current (log i_k) as a function of overpotential (η).

(E) Comparison of kinetic parameters (kinetic rate constant (k_0) and diffusion coefficient (D) of reported redox-active materials in RFB system: this work (blue stars) and reported RFBs (pink circles).

were unaffected by each other in any redox states in the mixed electrolyte system.[12,51] According to the CV results, the all-organic RFB exploiting the BMEPZ/FL redox couple is expected to offer the cell voltages of 1.21 and 2.00 V.

Characterization of BMEPZ Catholyte

We conducted bulk electrolysis and rotating disk electrode (RDE) experiments to investigate the intrinsic electrochemical properties of the newly synthesized BMEPZ molecule. Bulk electrolysis was appropriate to investigate the inherent redox ability and stability of BMEPZ under convection without considering the anolyte in the actual RFB system. As shown in Figure 2A, BMEPZ exhibits two distinct plateaus on charge and discharge at potentials consistent with the observations from the CV measurements. In addition, the measured capacity (1.573 mAh) was remarkably close to the theoretical value (1.608 mAh), indicating that all the BMEPZ molecules effectively contributed to the two-step reactions of each single-electron redox. Moreover, highly stable cycling was observed without any noticeable capacity fading, as shown in Figure 2B, implying that the multi-redox reactions of BMEPZ are reversible. The RDE tests revealed the kinetic properties of the BMEPZ and $BMEPZ^+$ species with respect to the mass-diffusion and charge-transfer rates. In the linear sweep voltammetry (LSV) curves, the mass-transfer-controlled limiting currents (i_L) increased with increasing rotation rate (ω) in the range of 300–1500 rpm (Figures S4A and S4B). Figure 2C shows that the linear relationship between i_L and the square root of ω was well-fitted by the Levich equation;[52] the diffusion coefficients (D) of BMEPZ and $BMEPZ^+$ were calculated to be 1.02 and 1.12 × 10^{-5} cm^2 s^{-1}, respectively (a detailed description of the calculations is provided in the

electrochemistry section of Experimental Procedures). The kinetic-controlled currents (i_k) at different overpotentials (η) were also determined by extrapolation in the Koutecký–Levich plots (Figures S4C and S4D).[52] The logarithms of the exchange currents (log i_0) were determined to be −3.65 for BMEPZ and −3.28 for $BMEPZ^+$ in the linearly fitted plots of log i_k versus η (Figure 2D), yielding kinetic rate constants (k_0) of 1.18×10^{-2} and 2.77×10^{-2} cm s^{-1}, respectively. Notably, even though BMEPZ is bulkier than DMPZ, the kinetics of BMEPZ were on par with or even faster than those of DMPZ (D of 1.58×10^{-5} and 8.82×10^{-6} cm^2 s^{-1}, respectively, and k_0 of 2.97×10^{-2} and 5.53×10^{-3} cm s^{-1}, respectively, for DMPZ and $DMPZ^+$).[37] In Figure 2E, the kinetic parameters for BMEPZ, $BMEPZ^+$, and FL (blue stars) are compared with those of previously reported materials for RFBs (pink circle dots) on a logarithmic scale. It is noteworthy that the BMEPZ/FL redox couple exceeds the others in terms of both mass- and charge-transfer kinetics, implying that the redox couple would be favorable for a low-polarization and high-efficiency RFB. In addition, a scan-rate dependent CV study was conducted to verify the reversibility of BMEPZ/FL redox couple. As shown in Figure S5, the current ratio between cathodic and anodic peaks of both BMEPZ and FL was almost unity in the CV curves, implying their superior reversibility. The redox couple showed the peak separations ranging from 80 to 100 mV with respect to the scan-rate. Furthermore, the Randles-Sevcik equation was used to determine their diffusion coefficients.[53] The diffusion coefficients of BMEPZ, $BMEPZ^+$, and FL were calculated to be 8.86×10^{-6}, 1.16×10^{-5}, and 1.05×10^{-5} cm^2 s^{-1}, respectively, which are consistent with those from the RDE study.

Raman spectroscopy and natural population analysis (NPA) were conducted to verify the redox mechanism of the BMEPZ molecule. In Figure 3A, the reversible changes of the local bonding of BMEPZ (pink areas) upon charging and discharging are shown. Notably, the peak changes mainly corresponded to the vibrational modes of C–N–C and C=C bonds in the reduced diazabutadiene motif (N–C=C–N), which is consistent with the previous observation for DMPZ (Table S1).[37,47] In addition, the NPA enabled visualization of the changes of the charge distribution of BMEPZ during the redox reaction. From the results for BMEPZ, $BMEPZ^+$, and $BMEPZ^{2+}$ (Figure S6), the change of the charge was plotted for each atom as colors ranging from white to pink, as shown in Figure 3B. The most drastic color changes were observed at the nitrogen atoms, followed by the conjugated carbons in the benzene rings, implying that the redox reaction of BMEPZ mainly occurs in the diazabutadiene motif. This finding supports the idea that the flexible side chains substituted to elevate the solubility did not affect the general redox mechanisms.

To explore the origin of the chemical stability of the BMEPZ molecule at all redox states in the given MeCN-based electrolyte, density functional theory (DFT) calculations were conducted for BMEPZ, $BMEPZ^+$, $BMEPZ^{2+}$, and MeCN. It was observed that the energy levels of the lowest unoccupied molecular orbital (LUMO) of BMEPZ and the singly occupied molecular orbital (SOMO) of the radical $BMEPZ^+$ were located above the highest occupied molecular orbital (HOMO) level of MeCN. More importantly, even the LUMO level of $BMEPZ^{2+}$ was higher than the HOMO level of MeCN, indicating that the electron transfer from MeCN to BMEPZ in any oxidation state during the battery operation is prohibited. Similarly, the electron transfer from BMEPZ in any oxidation state to MeCN is energetically unfavorable because the HOMO (or SOMO) levels of BMEPZ and $BMEPZ^{2+}$ (or $BMEPZ^+$) are lower than the LUMO level of MeCN. The above theoretical calculations indicate that parasitic side reactions based on electron transfer between BMEPZ and MeCN are less likely to occur during battery operation (Figure S7).

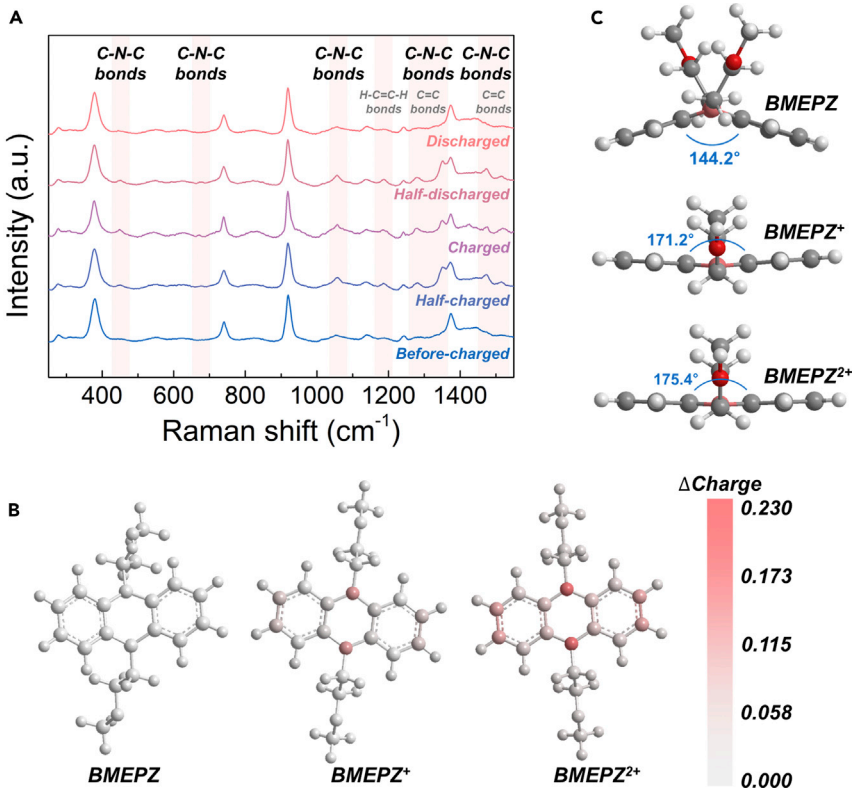

Figure 3. Investigation of Redox Mechanism of BMEPZ

(A) *Ex situ* Raman analysis for BMEPZ in catholyte, demonstrating the reversible appearance and disappearance of several peaks.

(B) NPA of BMEPZ, $BMEPZ^{+}$, and $BMEPZ^{2+}$. The depth of the pink color denotes the extent of the charge change.

(C) Molecular geometries of BMEPZ, $BMEPZ^{+}$, and $BMEPZ^{2+}$.

In addition, the structural changes in the optimized geometries of BMEPZ during the redox reactions were observed. As shown in Figure 3C, the neutral BMEPZ has bent conformation with an angle of 144.2° between the two phenyl ring planes. The radical cation and dication, in contrast, show almost planar geometries with the angles of 171.2° and 175.4°, respectively. It can be speculated that the planar molecular geometries of the radical cation and dication effectively delocalized the additional charges, leading to the remarkable redox stability of BMEPZ.[54,55] It is noteworthy that many p-type ROMs except BMEPZ tend to be very unstable when they are oxidized by two electrons, resulting in fast decay of the cycle performance.[13,31]

Electrochemical Performance of BMEPZ/FL Flow Cell

Cycling tests of flow cells employing BMEPZ as the catholyte and FL as the anolyte were performed using a custom flow cell (see the Experimental Procedures section for further details) to investigate the electrochemical performance in a near-practical system. Figure 4A presents a representative charge-discharge curve for the dilute condition of 0.05 M BMEPZ and 0.1 M FL in a supporting electrolyte of 0.5 M bis(trifluoromethane)sulfonimide lithium salt (LiTFSI) in MeCN at a current density of 20 mA cm^{-2}. The flow cell exhibited two well-defined plateaus at cell voltages of 1.2 and 2.0 V, which is consistent with the expectations from the CV curves in Figure 1B. The plateaus of the same length at each voltage indicate that the two single-electron

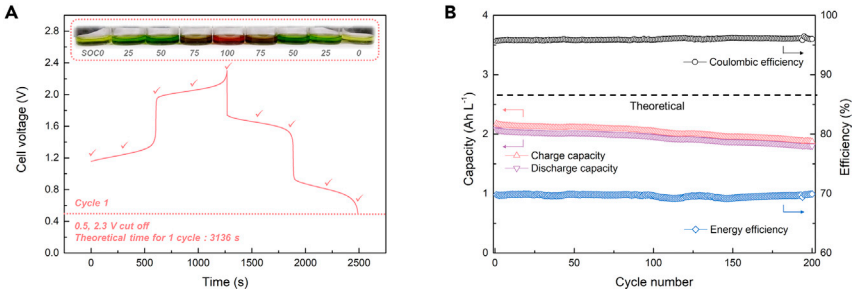

Figure 4. Electrochemical Performance of Flow Cell of 50 mM BMEPZ and 0.1 M FL

(A) Representative cell voltage versus time profile at a current density of 20 mA cm^{-2}. The inset shows the color change of the catholyte as a function of the SOC.

(B) Cycling efficiencies and capacities with respect to cycle number.

redox reactions of BMEPZ contribute equally to the cell capacity in the flow cell system. Additionally, we observed the color changes of the catholyte during redox reactions, which are presented as a function of the state of charge (SOC) with a step size of SOC 25 in Figure 4A. The color changes roughly occurred in two distinct stages, from yellow to green and from green to red, because of the double-redox reactions of BMEPZ, which could be quantitatively probed using UV-vis spectroscopy (Figure S8). The cycling efficiencies and capacity retention of the flow cell are plotted in Figure 4B. The cycling of the flow cell has a Coulombic efficiency of ~96% with an energy efficiency of ~70%, which were stably maintained over 200 cycles. Moreover, an initial discharge capacity of 2.08 Ah L^{-1} was achieved, which is close to the theoretical capacity of 2.67 Ah L^{-1} and yields a material utilization of ~80%. Note that the initial capacity could be retained over 200 cycles (cycling time of ~129 h) with a capacity retention of 99.94% per cycle and 70% of theoretical capacity could be achieved after 200 cycles (Figure S9). We attribute this highly robust cycle performance of the cell to the high stability of $BMEPZ^+$ radical cation in the electrolyte as well as the stable dication form of BMEPZ. Typically, organic radicals are often highly reactive and thus unstable, which is the key obstacle for improving the cycle performance in an organic flow battery. In contrast, it is noteworthy that the UV-vis spectra of $BMEPZ^+$ in the electrolyte were virtually unchanged over 24 h (Figure S10), indicating that $BMEPZ^+$ has superior radical stability.[12,56]

We next performed a demonstration of the flow cell under the near-saturation condition of BMEPZ to investigate the electrochemical behavior under practical cell conditions. In Figure 5A, additional charge-discharge curves for flow cells using 0.1 M and 0.4 M BMEPZ are presented. A proportional elevation of the capacity was observed with respect to the concentration, and stable cycling of 99.94% per cycle was achieved for the 0.1 M BMEPZ flow cell in Figure 5B. In addition, the 0.4 M BMEPZ flow cell was successfully demonstrated with a material utilization of ~75% during discharge and a respectable capacity retention of 99.3% per cycle in Figure 5C. Despite the superior stability of BMEPZ at all redox states, the capacity decay in concentrated cell was non-negligible. Since longer cycling time was needed for the concentrated cell at the same current density, more ROM molecules would cross over through the microporous separator, represented by the low Coulombic efficiency of 83%. Moreover, during the extended cycling time, the FL radical anions at the charged state might have more chance to decay because of their rather short lifetime.[12] It can thus be expected that the development of membrane which can suppress the cross-over issue and using more stable anolyte material would improve cycle life in the concentrated cell. For comparison of the

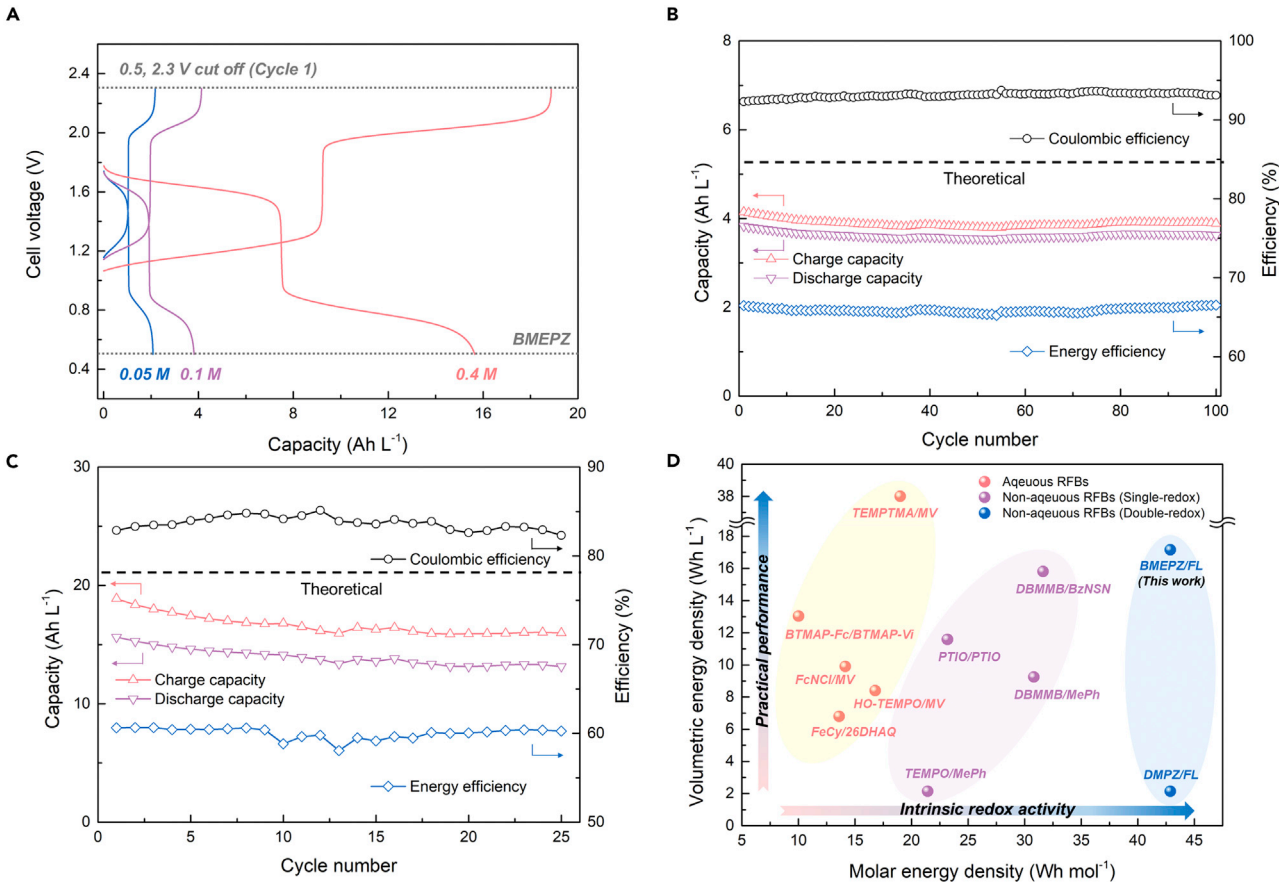

Figure 5. Electrochemical Performance of BMEPZ/FL Flow Cell at High Concentrations

(A) Typical charge-discharge curves at different concentrations.

(B) Cycling efficiencies and capacities for 0.1 M BMEPZ and 0.2 M FL with respect to cycle number.

(C) Cycling efficiencies and capacities for 0.4 M BMEPZ and 0.8 M FL with respect to cycle number.

(D) Energy density plot of typical redox-active materials in organic RFBs. The molar energy density is the volumetric energy density divided by the cycling concentration.

performance of the BMEPZ/FL flow cell with that of previously reported all-organic RFBs involving both aqueous and non-aqueous media, the theoretical energy densities of the RFBs at the cycling concentration are plotted in Figure 5D. The energy densities of the RFBs are presented with respect to the intrinsic activity of the redox couple (energy per mole) and its concentration in the solvent (energy per volume). With regard to the dynamic properties of solvents and cost issue, the molar energy density should be considered because ROMs with high molar energy densities are advantageous to deliver high energy densities using relatively low concentrations of ROMs. The figure shows that AORFBs (yellow areas) generally exhibit low intrinsic energy densities limited by the low cell voltage (<1.4 V); therefore, a high-concentration electrolyte is required to achieve a high volumetric energy density. For instance, Janoschka et al. demonstrated the high volumetric energy density (38 Wh L^{-1}), which is comparable to the vanadium RFBs, but it needed 2.0 M solutions of TEMPO derivative and methyl viologen.[40] In contrast, a relatively high molar energy density can be attained for NORFBs (purple areas) because of the wide electrochemical window. Furthermore, NORFBs using multi-redox ROMs present a promising pathway to realize high volumetric energy density with exceptionally high molar energy densities, as illustrated in blue areas. However, in practice, their

volumetric energy density rarely exceeds that of aqueous RFBs because of the relatively low cycling concentration limited by the dynamic properties of non-aqueous media and the lack of suitable membrane. As the multi-redox capability is combined with enhanced solubility in the BMEPZ/FL system, the volumetric energy density (~17 Wh L^{-1}) exceeded that of other NORFBs even at a lower concentration (~0.4 M), showing a great potential of multi-redox NORFB systems. It can be expected that further engineering to achieve solubility of phenazine derivatives over 1 M and the development of high-performance membrane for the non-aqueous system would enable the phenazine-based NORFB to outperform vanadium-based and aqueous organic systems.

Conclusions

We reported a multi-redox BMEPZ inspired by biosystems as a promising catholyte material with the highest energy density demonstrated for organic RFBs. This ROM undergoes two reversible redox reactions at high redox potentials of –0.29 and 0.50 V versus Fc/Fc^+ and exhibits outstanding electrochemical kinetics for the mass- and charge-transfer processes, retaining high solubility in non-aqueous media. An all-organic flow cell exploiting the BMEPZ/FL redox couple was successfully prepared with two well-defined voltage plateaus at 1.2 and 2 V and highly robust cycling owing to the remarkable chemical stability, delivering one of the highest energy density of reported NORFBs. Although further engineering of ROMs and the development of high-performance membrane are still needed for practical application of this system, these findings on a new multi-electron redox material combined with the high solubility provide a breakthrough in the realization of high-energy-density RFBs.

EXPERIMENTAL PROCEDURES

Preparation of Materials

MeCN (anhydrous) and FL were purchased from Sigma–Aldrich and used without further purification. The microporous separator (Celgard 4560) and LiTFSI were purchased from Wellcos (Korea) and TCI Chemicals (Japan) and were treated under vacuum at 70°C for 24 h to remove moisture. Tetrahydrofuran (THF) was distilled using sodium and benzophenone before use. All the other reagents and solvents were obtained from Sigma-Aldrich and Alfa Aesar Co. and used as received without further purification. All the glassware, syringes, magnetic stirring bars, and needles were thoroughly dried in a convection oven. The reactions were monitored using thin layer chromatography (TLC) using commercial TLC plates (silica gel 60 F254, Merck Co.).

Synthesis

Synthesis of 5,10-dihydrophenazine (1)

The 5,10-dihydrophenazine (**1**) was prepared following reported procedures.[57] Phenazine (3 g, 16.6 mmol) was dissolved in ethanol (75 mL), and the solution was heated to boiling. An aqueous solution (300 mL) containing $Na_2S_2O_4$ (30 g, 0.17 mol) was added to the boiling solution. The solution turned purple immediately after mixing; then, a greenish white precipitate formed. The precipitated solid was collected by filtration, washed with water, and dried in vacuo to afford 2.7 g of a greenish white solid. Because of its instability in air, the solid was stored under nitrogen without further purification and characterized.

Synthesis of 5,10-bis(2-methoxyethyl)-5,10-dihydrophenazine (2, BMEPZ)

In a flame-dried two-necked 100-mL round bottom flask, **1** (1 g, 5.5 mmol) was dissolved in freshly distilled THF (12 mL). To this solution, 1.6 M n-butyl lithium (n-BuLi) in hexane (9.5 mL, 15.4 mmol) was added dropwise over 30 min at room

temperature. After an orange precipitate was formed, 2-chloroethyl methyl ether (3.5 mL, 38.5 mmol) was added. Subsequently, the orange precipitate disappeared, forming a reddish-brown solution. The solution was stirred overnight, and the reaction mixture was then poured into water and extracted three times with ethyl acetate. The organic layer was dried over anhydrous $MgSO_4$ and purified using column chromatography on neutral alumina with ethyl acetate/n-hexane (1:19 v/v) as an eluent to give a light-yellow powder. Yield: 78.2% (1.28 g), ^{1}H-NMR (300 MHz, C_6D_6) δ(ppm): 6.60–6.57 (m, 4H), 6.31–6.28 (m, 4H), 3.43 (t, J = 6.3 Hz, 4H), 3.25 (t, J = 6.3 Hz, 4H), 2.99 (s, 6H). ^{13}C-NMR (125 MHz, C_6D_6) δ(ppm): 137.75, 111.84, 69.15, 59.03, 46.35. Anal. calc. for $C_{18}H_{22}N_2O_2$: C, 72.46; H, 7.43; N, 9.39; found: C, 72.42; H, 7.43; N, 9.38; HRMS (EI+): calc. for $C_{18}H_{22}N_2O_2$ (M^+), 298.1681; found, 298.1684 (Figure S11).

Characterization

^{1}H-NMR and ^{13}C-NMR spectra were recorded on a Bruker Avance-300 and Avance-500 NMR spectrometer, respectively. HRMS were obtained using a JEOL JMS-700 instrument. Elemental analysis was conducted using a Thermo Fisher Scientific Flash 2000 elemental analyzer.

In the solubility measurement, 30.2 mg of BMEPZ powder was fully dissolved in 2 mL MeCN to make a 0.05 M solution first. Then, to the solution, the same amount (30.2 mg) of BMEPZ powder was repeatedly added until it got saturated without further dissolution.

For the electrochemical measurements, the solutions were prepared and evaluated in an Ar-filled glove box under an inert atmosphere (<0.5 ppm O_2, H_2O). CV curves of DMPZ, BMEPZ, FL, and the mixture of BMEPZ and FL (10 mM each) were obtained using 0.1 M LiTFSI in MeCN as a supporting electrolyte. A three-electrode system (a Pt counter electrode, a $Ag/AgNO_3$ reference electrode, and Au working electrode) was employed, and a scan rate of 100 mV s^{-1} was used. Ferrocene (5 mM) was used as an internal reference.

For the bulk-electrolysis test, a commercially available bulk-electrolysis cell (MF-1056) was used. The cycling experiment used an electrolyte consisting of 1 mM BEMPZ and 0.5 M LiTFSI in MeCN (30 mL) and was stirred at 1,400 rpm. A three-electrode system (a Pt counter electrode, $Ag/AgNO_3$ reference electrode, and reticulated vitreous carbon working electrode) was employed at a current of 1.608 mA (1C).

For the RDE test, a three-electrode system (a Pt counter electrode, $Ag/AgNO_3$ reference electrode, and glassy carbon working electrode with 5-mm diameter) was employed for the LSV tests. The $BMEPZ^+$ solution was prepared by oxidizing the BMEPZ solution in the bulk-electrolysis experiment under a cut-off voltage of −0.11 V versus Fc/Fc^+. The working electrode was rotated from 300 to 1,500 rpm (in increments of 300 rpm) using a modulated speed rotator (AFMSRX; PINE). The LSV tests were conducted with 1.0 mM ROMs in 0.5 M LiTFSI in MeCN at a scan rate of 5 mV s^{-1}. The kinematic viscosity (υ) of the 0.5 M LiTFSI in MeCN was measured to be 0.59 $mm^2\ s^{-1}$ following the standard test method ASTM D445 in Korea Polymer Testing & Research Institute (Koptri, Korea). Using the slopes of the linearly fitted Levich plots (Figure 2C) and the Levich equation (Equation 1), the diffusion coefficients (D) of the ROMs were calculated (the slopes of BMEPZ and $BMEPZ^+$ were determined to be 1.30×10^{-5} and 1.38×10^{-5} A $rad^{-1/2}\ s^{1/2}$, respectively). Using the Koutecký–Levich equation (Equation 2), Koutecký–Levich plots (Figures S4C and S4D) were obtained

at different overpotentials, and the kinetic rate constants of the ROMs were calculated using Equation 3.

$$i_L = 0.62nFAD^{2/3}\omega^{1/2}\upsilon^{-1/6}C_0 \quad \text{(Equation 1)}$$

$$\frac{1}{i} = \frac{1}{i_k} + \frac{1}{0.62nFAD^{2/3}\omega^{1/2}\upsilon^{-1/6}C_0} \quad \text{(Equation 2)}$$

$$i_0 = nFAk_0C_0 \quad \text{(Equation 3)}$$

Here, n is the number of electrons transferred ($n = 1$), F is the Faraday constant ($F = 96,485\ C\ mol^{-1}$), A is the electrode area ($A = 0.2\ \ cm^2$), and C_0 is the concentration of the ROM ($C_0 = 1.0\ \ mM$).

For the scan-rate dependence CV study, CV curves of BMEPZ and FL (10 mM each) were obtained using 0.5 M LiTFSI in MeCN as a supporting electrolyte at the following scan-rates: 25, 50, 100, 200, and 300 mV s^{-1}. Randles-sevcik equation (Equation 4) was used to calculate the diffusion coefficients of ROM.

$$i_p = 0.4463nFAC\left(\frac{nFsD}{RT}\right)^{\frac{1}{2}} \quad \text{(Equation 4)}$$

Here, A is the electrode area ($A = 7.07\ \ mm^2$), C is the concentration of the ROM ($C = 10\ \ mM$), and s is the scan-rate, respectively.

Raman spectra (LabRAM HR Evolution, Horiba) were recorded using capillary tubes (inner diameter of 1.1–1.2 mm) with continuous-wave linearly polarized lasers (wavelength: 532 nm). The laser beam was focused using a 50× objective lens, resulting in a spot diameter of approximately 1 μm. The acquisition time and number of accumulations were 10 s and 5, respectively.

For the UV-vis spectroscopy analysis, absorption spectra of the electrolytes in the positive electrode compartment (diluted in MeCN, 5% v/v) were obtained using a UV-vis spectrometer (Agilent Technologies, Cary 5000) with an optical glass cuvette (Quartz; Hellma). Electrolytes containing 10 mM BMEPZ and 20 mM FL in the supporting electrolyte of 0.5 M LiTFSI in MeCN were used.

Computational Details

Spin-unrestricted density functional theory (DFT)-type calculations were performed using the Gaussian 09 package,[58] including geometry optimization, energy evaluation, eigenvalue calculation, NPA calculation, and vibration property prediction for each molecule. The Becke–Lee–Yang–Parr (B3LYP) hybrid exchange-correlation functional[59–61] and triple-zeta valence polarization (TZVP) basis set[62,63] were used for the entire calculation, which have been demonstrated to reproduce experimental results well.[37,47,64,65] To model the solvation environment of acetonitrile (dielectric constant = 38.8), the polarizable continuum model (PCM) scheme, implicit solvation model, was introduced for the entire calculation. The LUMO and SOMO denote the adiabatic LUMO and SOMO.

Flow Cell Test

A custom flow cell with backing plates (polyethylene-coated fiber glass), flow fields (polytetrafluoroethylene (PTFE)), and gaskets (PTFE) was fabricated using materials purchased from ILDO F&C (Korea). The flow cells were assembled with carbon felt (XF30A; TOYOBO, Korea) as electrodes at both the anode and cathode side with four pieces of microporous separators (Celgard 4560) sandwiched in between.

The active size of the flow cell was 2.0-cm wide × 2.0-cm long (4 cm^2), and a norprene tubing (Masterflex) was used. The mixed electrolytes (13 mL in each half-cell side) containing both BMEPZ and FL with the supporting electrolyte of 0.5 M LiTFSI in MeCN were flowed through the felt electrodes at a flow rate of 80 mL min^{-1} using a pump (ShenChen). In the case of 0.4 M BMEPZ cell test, 0.8 M FL and 1.0 M LiTFSI were used as the anolyte and the supporting electrolyte, respectively. Flow cell tests were performed at a current density of 20 mA cm^{-2} in constant-current mode using a battery test system (WBCS 3000; WonA Tech, Korea), and free 20 cycles (5 cycles for 0.4 M BMEPZ and 0.8 M FL cell test) were conducted in advance for initial equilibration of the flow setup. The volumetric energy density was calculated based on the entire electrolyte volume (26 mL).

SUPPLEMENTAL INFORMATION

Supplemental Information can be found online at https://doi.org/10.1016/j.chempr.2019.07.006.

ACKNOWLEDGMENTS

We especially thank Dr. Minah Lee (Korea Institute of Science and Technology) and Dr. Jihyun Hong (Korea Institute of Science and Technology) for providing inspiration of using biomaterials as energy storage materials. This work was supported by the National Research Foundation of Korea (NRF) grant funded by the Korean Government (MSIP) (2015R1A2A1A10055991), Lotte Chemical, Creative Materials Discovery Program through the National Research Foundation of Korea (NRF) funded by the Ministry of Science, ICT and Future Planning (NRF-2017M3D1A1039553), and Presidential Post-Doc. Fellowship Program through the National Research Foundation (NRF) of Korea funded by the Ministry of Education [2016R1A6A3A04008134(RIAM0417-20180002)].

AUTHOR CONTRIBUTIONS

G.K. designed the experiments with help from M.H.L., S.L., S.-K.J., K.K., and J.K. K.L. performed the organic synthesis with help from S.Y.P. The computations were performed by B.L. K.K. and J.E.K supervised the overall research. All authors discussed the experiments and final manuscript.

DECLARATION OF INTERESTS

The authors declare no competing interests.

Received: March 29, 2019
Revised: June 14, 2019
Accepted: July 12, 2019
Published: August 19, 2019

REFERENCES

1. Yang, Z., Zhang, J., Kintner-Meyer, M.C.W., Lu, X., Choi, D., Lemmon, J.P., and Liu, J. (2011). Electrochemical energy storage for green grid. Chem. Rev. *111*, 3577–3613.

2. Dunn, B., Kamath, H., and Tarascon, J.M. (2011). Electrical energy storage for the grid: a battery of choices. Science *334*, 928–935.

3. Soloveichik, G.L. (2015). Flow batteries: current status and trends. Chem. Rev. *115*, 11533–11558.

4. Wang, Y., He, P., and Zhou, H. (2012). Li-redox flow batteries based on hybrid electrolytes: at the cross road between Li-ion and redox flow batteries. Adv. Energy Mater. *2*, 770–779.

5. Darling, R.M., Gallagher, K.G., Kowalski, J.A., Ha, S., and Brushett, F.R. (2014). Pathways to low-cost electrochemical energy storage: a comparison of aqueous and nonaqueous flow batteries. Energy Environ. Sci. *7*, 3459–3477.

6. Nguyen, T., and Savinell, R.F. (2010). Flow batteries. Electrochem. Soc. Interface *19*, 54–56.

7. Noack, J., Roznyatovskaya, N., Herr, T., and Fischer, P. (2015). The chemistry of redox-flow batteries. Angew. Chem. Int. Ed. Engl. *54*, 9776–9809.

8. Sevov, C.S., Samaroo, S.K., and Sanford, M.S. (2017). Cyclopropenium salts as cyclable, high-potential catholytes in nonaqueous media. Adv. Energy Mater. *7*.

9. Winsberg, J., Hagemann, T., Janoschka, T., Hager, M.D., and Schubert, U.S. (2017). Redox-flow batteries: from metals to organic redox-active materials. Angew. Chem. Int. Ed. Engl. *56*, 686–711.

10. Wei, X., Pan, W., Duan, W., Hollas, A., Yang, Z., Li, B., Nie, Z., Liu, J., Reed, D., Wang, W., et al. (2017). Materials and systems for organic redox flow batteries: status and challenges. ACS Energy Lett. *2*, 2187–2204.

11. Park, M., Ryu, J., Wang, W., and Cho, J. (2017). Material design and engineering of next-generation flow-battery technologies. Nat. Rev. Mater. *2*, 16080.

12. Wei, X., Xu, W., Huang, J., Zhang, L., Walter, E., Lawrence, C., Vijayakumar, M., Henderson, W.A., Liu, T., Cosimbescu, L., et al. (2015). Radical compatibility with nonaqueous electrolytes and its impact on an all-organic redox flow battery. Angew. Chem. Int. Ed. Engl. *54*, 8684–8687.

13. Milshtein, J.D., Kaur, A.P., Casselman, M.D., Kowalski, J.A., Modekrutti, S., Zhang, P.L., Harsha Attanayake, N.H., Elliott, C.F., Parkin, S.R., Risko, C., et al. (2016). High current density, long duration cycling of soluble organic active species for non-aqueous redox flow batteries. Energy Environ. Sci. *9*, 3531–3543.

14. Ding, Y., Zhao, Y., Li, Y., Goodenough, J.B., and Yu, G. (2017). A high-performance all-metallocene-based, non-aqueous redox flow battery. Energy Environ. Sci. *10*, 491–497.

15. Duan, W., Huang, J., Kowalski, J.A., Shkrob, I.A., Vijayakumar, M., Walter, E., Pan, B., Yang, Z., Milshtein, J.D., and Li, B. (2017). Wine-dark sea in an organic flow battery: storing negative charge in 2,1,3-benzothiadiazole radicals leads to improved cyclability. ACS Energy Lett. *2*, 1156–1161.

16. Ding, Y., Li, Y., and Yu, G. (2016). Exploring bio-inspired quinone-based organic redox flow batteries: a combined experimental and computational study. Chem *1*, 790–801.

17. Chen, H., Zhou, Y., and Lu, Y.-C. (2018). Lithium-organic nanocomposite suspension for high-energy-density redox flow batteries. ACS Energy Lett. *3*, 1991–1997.

18. Zhao, Q., Zhu, Z., and Chen, J. (2017). Molecular engineering with organic carbonyl electrode materials for advanced stationary and redox flow rechargeable batteries. Adv. Mater. *29*.

19. Kang, N., Park, J.H., Choi, J., Jin, J., Chun, J., Jung, I.G., Jeong, J., Park, J.G., Lee, S.M., Kim, H.J., et al. (2012). Nanoparticulate iron oxide tubes from microporous organic nanotubes as stable anode materials for lithium ion batteries. Angew. Chem. Int. Ed. Engl. *51*, 6626–6630.

20. Benniston, A.C., Hagon, J., He, X., Yang, S., and Harrington, R.W. (2012). Spring open two-plus-two electron storage in a disulfide-strapped methyl viologen derivative. Org. Lett. *14*, 506–509.

21. Song, Z., and Zhou, H. (2013). Towards sustainable and versatile energy storage devices: an overview of organic electrode materials. Energy Environ. Sci. *6*, 2280–2301.

22. Lee, S., Kwon, G., Ku, K., Yoon, K., Jung, S.K., Lim, H.D., and Kang, K. (2018). Recent progress in organic electrodes for Li and Na rechargeable batteries. Adv. Mater. *30*.

23. Hu, B., and Liu, T.L. (2018). Two electron utilization of methyl viologen anolyte in nonaqueous organic redox flow battery. J. Energy Chem. *27*, 1326–1332.

24. Lin, K., Chen, Q., Gerhardt, M.R., Tong, L., Kim, S.B., Eisenach, L., Valle, A.W., Hardee, D., Gordon, R.G., Aziz, M.J., et al. (2015). Alkaline quinone flow battery. Science *349*, 1529–1532.

25. Liu, T., Wei, X., Nie, Z., Sprenkle, V., and Wang, W. (2016). A total organic aqueous redox flow battery employing a low cost and sustainable methyl viologen anolyte and 4-HO-TEMPO catholyte. Adv. Energy Mater. *6*.

26. Luo, J., Hu, B., Debruler, C., and Liu, T.L. (2018). A π-conjugation extended viologen as a two-electron storage anolyte for total organic aqueous redox flow batteries. Angew. Chem. Int. Ed. Engl. *57*, 231–235.

27. Yang, Z., Tong, L., Tabor, D.P., Beh, E.S., Goulet, M.A., De Porcellinis, D., Aspuru-Guzik, A., Gordon, R.G., and Aziz, M.J. (2018). Alkaline benzoquinone aqueous flow battery for large-scale storage of electrical energy. Adv. Energy Mater. *8*.

28. Huskinson, B., Marshak, M.P., Suh, C., Er, S., Gerhardt, M.R., Galvin, C.J., Chen, X., Aspuru-Guzik, A., Gordon, R.G., and Aziz, M.J. (2014). A metal-free organic–inorganic aqueous flow battery. Nature *505*, 195–198.

29. Kwabi, D.G., Lin, K., Ji, Y., Kerr, E.F., Goulet, M.-A., De Porcellinis, D., Tabor, D.P., Pollack, D.A., Aspuru-Guzik, A., Gordon, R.G., et al. (2018). Alkaline quinone flow battery with long lifetime at pH 12. Joule *2*, 1894–1906.

30. Zhang, C., Zhang, L., Ding, Y., Peng, S., Guo, X., Zhao, Y., He, G., and Yu, G. (2018). Progress and prospects of next-generation redox flow batteries. Energy Storage Mater. *15*, 324–350.

31. Wei, X., Duan, W., Huang, J., Zhang, L., Li, B., Reed, D., Xu, W., Sprenkle, V., and Wang, W. (2016). A high-current, stable nonaqueous organic redox flow battery. ACS Energy Lett. *1*, 705–711.

32. Wei, X., Xu, W., Vijayakumar, M., Cosimbescu, L., Liu, T., Sprenkle, V., and Wang, W. (2014). TEMPO-based catholyte for high-energy density nonaqueous redox flow batteries. Adv. Mater. *26*, 7649–7653.

33. Zhang, J., Corman, R.E., Schuh, J.K., Ewoldt, R.H., Shkrob, I.A., and Zhang, L. (2018). Solution properties and practical limits of concentrated electrolytes for nonaqueous redox flow batteries. J. Phys. Chem. C *122*, 8159–8172.

34. Li, Z., and Lu, Y.-C. (2018). Redox flow batteries: want more electrons? Go organic! Chem *4*, 2020–2021.

35. Kim, H.-s., Lee, K.-J., Han, Y.-K., Ryu, J.H., and Oh, S.M. (2017). A comparative study on the solubility and stability of p-phenylenediamine-based organic redox couples for non-aqueous flow batteries. J. Power Sources *348*, 264–269.

36. Kowalski, J.A., Casselman, M.D., Kaur, A.P., Milshtein, J.D., Elliott, C.F., Modekrutti, S., Attanayake, N.H., Zhang, N., Parkin, S.R., Risko, C., et al. (2017). A stable two-electron-donating phenothiazine for application in nonaqueous redox flow batteries. J. Mater. Chem. A *5*, 24371–24379.

37. Kwon, G., Lee, S., Hwang, J., Shim, H.-S., Lee, B., Lee, M.H., Ko, Y., Jung, S.-K., Ku, K., Hong, J., et al. (2018). Multi-redox molecule for high-energy redox flow batteries. Joule *2*, 1771–1782.

38. Li, L., Kim, S., Wang, W., Vijayakumar, M., Nie, Z., Chen, B., Zhang, J., Xia, G., Hu, J., Graff, G., et al. (2011). A stable vanadium redox-flow battery with high energy density for large-scale energy storage. Adv. Energy Mater. *1*, 394–400.

39. Kear, G., Shah, A.A., and Walsh, F.C. (2012). Development of the all-vanadium redox flow battery for energy storage: a review of technological, financial and policy aspects. Int. J. Energy Res. *36*, 1105–1120.

40. Janoschka, T., Martin, N., Hager, M.D., and Schubert, U.S. (2016). An aqueous redox-flow battery with high capacity and power: the TEMPTMA/MV system. Angew. Chem. Int. Ed. Engl. *55*, 14427–14430.

41. Beifuss, U., Tietze, M., Bäumer, S., and Deppenmeier, U. (2000). Methanophenazine: structure, total synthesis, and function of a new cofactor from methanogenic archaea. This work was supported by the Deutsche Forschungsgemeinschaft (Sonderforschungsbereich 416; grants De 488/6-1 and De 488/4-2) and the Fonds der Chemischen Industrie. We are grateful to Drs. J. Paust and H. Jaedicke (BASF AG, Ludwigshafen) and Dr. R. K. Müller (Hoffmann-La Roche Ltd., Basel) for generously providing chemicals. Angew. Chem. Int. Ed. Engl. *39*, 2470–2472.

42. Pierson, L.S., and Pierson, E.A. (2010). Metabolism and function of phenazines in bacteria: impacts on the behavior of bacteria in the environment and biotechnological processes. Appl. Microbiol. Biotechnol. *86*, 1659–1670.

43. Hollas, A., Wei, X., Murugesan, V., Nie, Z., Li, B., Reed, D., Liu, J., Sprenkle, V., and Wang, W. (2018). A biomimetic high-capacity phenazine-based anolyte for aqueous organic redox flow batteries. Nat. Energy *3*, 508–514.

44. Rada, B., and Leto, T.L. (2013). Pyocyanin effects on respiratory epithelium: relevance in Pseudomonas aeruginosa airway infections. Trends Microbiol. *21*, 73–81.

45. Tietze, M., Beuchle, A., Lamla, I., Orth, N., Dehler, M., Greiner, G., and Beifuss, U. (2003). Redox potentials of methanophenazine and CoB-S-S-CoM, factors involved in electron transport in methanogenic archaea. ChemBioChem *4*, 333–335.

46. Wang, Y., and Newman, D.K. (2008). Redox reactions of phenazine antibiotics with ferric (hydr) oxides and molecular oxygen. Environ. Sci. Technol. *42*, 2380–2386.

47. Lee, M., Hong, J., Lee, B., Ku, K., Lee, S., Park, C.B., and Kang, K. (2017). Multi-electron redox phenazine for ready-to-charge organic batteries. Green Chem. *19*, 2980–2985.

48. Zhang, J., Yang, Z., Shkrob, I.A., Assary, R.S., Tung, S.o., Silcox, B., Duan, W., Zhang, J., Su, C.C., Hu, B., et al. (2017). Annulated

dialkoxybenzenes as catholyte materials for non-aqueous redox flow batteries: achieving high chemical stability through bicyclic substitution. Adv. Energy Mater. *7*.

49. Kowalski, J.A., Su, L., Milshtein, J.D., and Brushett, F.R. (2016). Recent advances in molecular engineering of redox active organic molecules for nonaqueous flow batteries. Curr. Opin. Chem. Eng. *13*, 45–52.

50. Wang, W., Xu, W., Cosimbescu, L., Choi, D., Li, L., and Yang, Z. (2012). Anthraquinone with tailored structure for a nonaqueous metal–organic redox flow battery. Chem. Commun. (Camb.) *48*, 6669–6671.

51. Wei, X., Li, L., Luo, Q., Nie, Z., Wang, W., Li, B., Xia, G.-G., Miller, E., Chambers, J., and Yang, Z. (2012). Microporous separators for Fe/V redox flow batteries. J. Power Sources *218*, 39–45.

52. Bard, A.J., and Faulkner, L.R. (2002). Fundamentals and Applications (Wiley).

53. Compton, R.G., and Banks, C.E. (2011). Understanding Voltammetry (World Scientific).

54. Chiykowski, V.A., Lam, B., Du, C., and Berlinguette, C.P. (2017). Comparative analysis of triarylamine and phenothiazine sensitizer donor units in dye-sensitized solar cells. Chem. Commun. (Camb.) *53*, 2367–2370.

55. Narayana, K.A., Casselman, M.D., Elliott, C.F., Ergun, S., Parkin, S.R., Risko, C., and Odom, S.A. (2015). N-substituted phenothiazine derivatives: how the stability of the neutral and radical cation forms affects overcharge performance in lithium-ion batteries. ChemPhysChem *16*, 1179–1189.

56. Armstrong, C.G., and Toghill, K.E. (2018). Stability of molecular radicals in organic non-aqueous redox flow batteries: a mini review. Electrochem. Commun. *91*, 19–24.

57. Sugimoto, A., Kotani, T., Tsujimoto, J., and Yoneda, S. (1989). Preparation and properties of electron donor acceptor complexes of the compounds having capto-dative substituents. J. Heterocycl. Chem. *26*, 435–438.

58. Frisch, M.J., Trucks, G., Schlegel, H.B., Scuseria, G., Robb, M., Cheeseman, J., Scalmani, G., Barone, V., Mennucci, B., and Petersson, G. (2009). Gaussian 09, revision A. 1, *27* (Gaussian Inc.), p. 34.

59. Lee, C., Yang, W., and Parr, R.G. (1988). Development of the Colle-Salvetti correlation-energy formula into a functional of the electron density. Phys. Rev. B Condens. Matter *37*, 785–789.

60. Becke, A.D. (1993). Density-functional thermochemistry. III. The role of exact exchange. J. Chem. Phys. *98*, 5648–5652.

61. Stephens, P.J., Devlin, F.J., Chabalowski, C.F., and Frisch, M.J. (1994). Ab initio calculation of vibrational absorption and circular dichroism spectra using density functional force fields. J. Phys. Chem. *98*, 11623–11627.

62. Schäfer, A., Huber, C., and Ahlrichs, R. (1994). Fully optimized contracted Gaussian basis sets of triple zeta valence quality for atoms Li to Kr. J. Chem. Phys. *100*, 5829–5835.

63. Klaumünzer, B., Kröner, D., and Saalfrank, P. (2010). (TD-)DFT calculation of vibrational and vibronic spectra of riboflavin in solution. J. Phys. Chem. B *114*, 10826–10834.

64. Lim, H.-D., Lee, B., Zheng, Y., Hong, J., Kim, J., Gwon, H., Ko, Y., Lee, M., Cho, K., and Kang, K. (2016). Rational design of redox mediators for advanced Li–O_2 batteries. Nat. Energy *1*, 16066.

65. Hong, J., Lee, M., Lee, B., Seo, D.-H., Park, C.B., and Kang, K. (2014). Biologically inspired pteridine redox centres for rechargeable batteries. Nat. Commun. *5*, 5335.